A New Polarimetric Persistent Scatterer Interferometry Method Using Temporal Coherence Optimization

Zahra Sadeghi[ID], Mohammad Javad Valadan Zoej[ID], Andrew Hooper[ID], *Senior Member, IEEE*, and Juan M. Lopez-Sanchez, *Senior Member, IEEE*

Abstract—While polarimetric persistent scatterer InSAR (PSI) is an effective technique for increasing the number and quality of selected PS pixels, existing methods are suboptimal; a polarimetric channel combination is selected for each pixel based either on amplitude, which works well only for high-amplitude scatterers such as man-made structures, or on the assumption that pixels in a surrounding window all have the same scattering mechanism. In this paper, we present a new polarimetric PSI method in which we use a phase-based criterion to select the optimal channel for each pixel, which can work well even in nonurban environments. This algorithm is based on polarimetric optimization of temporal coherence, as defined in the Stanford Method for PS (StaMPS), to identify the scatterers with stable phase characteristics. We form all possible copolar and cross-polar interferograms from the available polarimetric channels and find the optimum coefficients for each pixel using defined search spaces to optimize the temporal coherence. We apply our algorithm, PolStaMPS, to an area in the Tehran basin that is covered primarily by vegetation. Our results confirm that the algorithm substantially improves on StaMPS performance, increasing the number of PS pixels by 48%, 80%, and 82% with respect to HH+VV, VV, and HH channels, respectively, and increasing the signal-to-noise ratio of selected pixels.

Index Terms—Polarimetric persistent scatterer InSAR (PSI), Stanford Method for PS (StaMPS), temporal coherence.

I. INTRODUCTION

PERSISTENT scatterer InSAR (PSI) is a well-known technique to address decorrelation and atmospheric noise in conventional interferometry. This method identifies only those scatterers which display coherent scattering behavior over time, known as persistent scatterers (PSs). A PSI algorithm was outlined first by Ferretti *et al.* [1], [2] with further algorithms quickly following [3]–[6]. In these algorithms, an initial set of PS pixels are identified by analysis of their amplitude scintillations in a series of coregistered SLC images and then

refined based on the match of their phase with a predefined deformation model. Thus, in general, only bright scatterers with a deformation behavior close to the assumed model are identified as PS pixels, and these algorithms work best where there are large numbers of man-made structures. Moreover, small baseline SAR differential interferometry approaches were presented by [7] and [8] based on the appropriate combination of different interferograms produced by data pairs with small orbital separation (baseline) in order to limit the spatial decorrelation. In these methods, coherent pixels are selected through spatial coherence estimation.

An alternative PSI method was put forward by [9] to identify large numbers of PS pixels in all terrains, including nonurban areas that lack man-made structures. This approach uses the spatial correlation of phase for identification of PS pixels. The parameter used to characterize phase stability in this approach is similar to a measure of coherence in time [10] and we refer to it as temporal coherence [9]. The ensemble phase coherence defined by [2], is not quite the same as the temporal coherence we refer to, as it requires a predefined deformation model.

Before the launch of radar sensors operating with a polarimetric configuration, SAR interferometry applications had been limited to a single polarimetric channel. Radar polarimetry is a valuable technique for the extraction of geophysical parameters from SAR images [11], [12]. Varying approaches to achieve this are based either on the statistical analysis of the polarimetric information [13], [14] or on scattering models, which provide an understanding of the physics of the scattering process [15]–[17]. Therefore, the introduction of polarimetric techniques in interferometric applications can improve performance of SAR interferometry. A general formulation for coherent conventional interferometry using polarimetry was introduced by Cloude and Papathanassiou [18]. This method sets up a spatial coherence optimization problem using different polarimetric channels, and then solves it to obtain the optimum linear combination of channels that leads to the best phase estimates. The decorrelation terms are decreased with the spatial coherence optimization, and signal-to-noise ratio is therefore increased [19]. Another spatial coherence optimization method was proposed by Colin *et al.* [20]. This approach optimizes the coherence using the same complex unitary vector for both antennae. This coherence is called single-mechanism coherence. Given a multibaseline data set in this method, coherence can be optimized independently for every baseline. This can lead to identification of different

dominant scattering centers depending on the chosen baseline. A more robust polarimetric optimization approach to find the most coherent and dominant scatterer is a simultaneous optimization of multibaseline coherence, a technique first outlined by Neumann *et al.* [19]. This approach generally leads to lower coherence magnitudes, but the corresponding linear combination of channels and their interferometric phases are estimated on the basis of all the available data and thus more accurately.

As density and quality of PS pixels are important factors in PSI algorithms, the concept of polarimetric optimization in the PSI algorithms was proposed in [21] and [22] with zero-baseline ground-based SAR (GB-SAR) data, to improve the number of reliable pixel candidates. In [21], the simplest coherence optimization approach is performed based on the selection of the polarimetric channel with the highest average coherence value. A polarimetric PSI approach, known as exhaustive search polarimetric optimization (ESPO), using spaceborne data set was presented first by Navarro-Sanchez *et al.* [23]. This method finds the optimal weights for each available polarimetric channel to obtain an optimum combination of those channels that maximizes the PS selection criterion. A study of the different polarimetric optimization techniques using both zero-baseline and multi-baseline data was carried out by Iglesias *et al.* [24]. The main goal was the exploitation of the available polarimetric optimization methods, in the framework of differential interferometry, to improve the density and quality of PS pixels. Moreover, Sadeghi *et al.* [25] compared the efficiency of different multibaseline polarimetric optimization techniques in terms of increasing the number of PS pixels and the signal-to-noise ratio, and also presented an enhanced multibaseline coherence optimization method. It should be noted that the use of polarimetric SAR data entails two main drawbacks when compared to conventional single-polarimetric data: an increase in the amount of data to be processed (proportional to the number of polarimetric channels) and a reduction in the size of the images in the swath direction (hence the spatial coverage) due to the doubled pulse repetition frequency required to acquire fully polarimetric data.

Polarimetric PSI implementations, up to now, either optimize amplitude-based criteria for identification of PS pixels [23], [24], [26], [27], or select the polarimetric channel combination that maximizes the ensemble coherence of surrounding pixels [24]–[26]. The former approach can be quite successful for bright scatterers, such as buildings, but less for natural PS. A limitation of the latter approach is the common failure of the assumption that PS pixels are surrounded by scatterers with the same scattering properties, which leads to nonoptimal weights for the polarimetric channels, and to a loss of spatial resolution. In this paper, we present a new method, Polarimetric Stanford Method for PS (PolStaMPS), which uses polarimetric optimization of temporal coherence to increase the number of selected PS pixels in all terrains, with or without buildings. We implement the temporal coherence optimization after computing different interferogram channels for each master and slave image. The temporal coherence optimization method was inspired by ESPO, as it finds the weights for each interferogram channels over search spaces. PolStaMPS codes

will be included in the next release of StaMPS/MTI, with full instructions added to the manual.

This paper is organized as follows. Section II contains the basic principles of polarimetric interferometry and a brief review of ESPO, which is a polarimetric PS interferometry method. The concept of temporal coherence in StaMPS is introduced in Section III, followed by our new algorithm for optimization of the temporal coherence, PolStaMPS, in Section IV. Section V describes the test site and the available dual-polarimetric data set to evaluate the new algorithm. In Section VI, experimental results of PolStaMPS are shown and discussed. Finally, the main conclusions are summarized in Section VII.

II. POLARIMETRIC INTERFEROMETRY

Since there is a vector value for each pixel instead of a scalar one, polarimetric interferometry can be referred to as vector interferometry [18]. The general formulation is defined in Section II-A. One of the most effective polarimetric PSI algorithms up to now, ESPO, was presented in [26]. This technique was formulated for two different criteria of PS selection to increase the number of PS pixels, which are amplitude dispersion index and average spatial coherence. A brief overview of this method is presented in Section II-B.

A. General Formulation

A general formulation for polarimetric SAR interferometry, presented in full by Cloude and Papathanassiou [18], is reviewed in this section. Fully polarimetric radar systems measure a 2×2 complex scattering matrix [S] for each pixel in an image [28]. Through vectorization of the scattering matrix, a coherent scattering vector $\underline{k}$ can be extracted to generalize interferometric phase and spatial coherence. Using Pauli basis matrices, the scattering vector for each pixel can be found as [18]

$$\underline{k} = \frac{1}{\sqrt{2}}[S^{\text{HH+VV}}, S^{\text{HH}-VV}, 2S^{HV}]^T \tag{1}$$

where T indicates the matrix transposition operation, and S^{ij} ($i, j =$ H or V) is the complex scattering coefficient for j transmitted and i received polarization in the HV polarization basis. In the case of dual-polarization interferometry, considering there is no data from the cross-polar channel, as provided by TerraSAR-X, the scattering vector changes to

$$\underline{k} = \frac{1}{\sqrt{2}}[S^{\text{HH+VV}}, S^{\text{HH}-VV}]^T. \tag{2}$$

Using the outer product formed from the scattering vectors $\underline{k}_m$ and $\underline{k}_s$ for master and slave images, a 4×4 matrix can be defined as

$$\mathbf{T}_4 = \begin{bmatrix} \mathbf{T}_{mm} & \mathbf{\Omega}_{ms} \\ \mathbf{\Omega}_{ms}^{\mathbf{H}} & \mathbf{T}_{ss} \end{bmatrix} \tag{3}$$

where H stands for conjugate transpose, and $\mathbf{T}_{mm}$, $\mathbf{T}_{ss}$, and $\mathbf{\Omega}_{ms}$ are 2×2 complex matrices given by

$$\mathbf{T}_{mm} = \langle \underline{k}_m \underline{k}_m^H \rangle$$
$$\mathbf{T}_{ss} = \langle \underline{k}_s \underline{k}_s^H \rangle$$
$$\mathbf{\Omega}_{ms} = \langle \underline{k}_m \underline{k}_s^H \rangle. \tag{4}$$

This article has been accepted for inclusion in a future issue of this journal. Content is final as presented, with the exception of pagination.

SADEGHI *et al.*: NEW POLARIMETRIC PS INTERFEROMETRY METHOD

3

In order to extend standard SAR interferometry, which uses a scalar formulation, into a vector formulation, two normalized complex vectors $\underline{\omega}_m$ and $\underline{\omega}_s$ for master and slave images are introduced. These vectors can be called projection vectors and interpreted as linear combination of channels. The scalar complex value for each pixel can be defined as $\mu = \underline{\omega}^H \underline{k}$, which is a linear combination of the elements of $\underline{k}$. The vector interferogram is obtained as

$$\mu_m \mu_s^* = \left(\underline{\omega}_m^H \underline{k}_m\right)\left(\underline{\omega}_s^H \underline{k}_s\right)^H = \underline{\omega}_m^H \Omega_{ms} \underline{\omega}_s \qquad (5)$$

where $*$ is the conjugate operation. The interferometric phase can be extracted using

$$\varphi_{\text{int}} = \arg\left(\underline{\omega}_m^H \Omega_{ms} \underline{\omega}_s\right). \qquad (6)$$

Optimum values of the projection vectors can be found through polarimetric optimization of spatial coherence. The generalised vector expression for the spatial coherence ρ is given by

$$\rho = \frac{\left|E\left(\underline{\omega}_m^H \Omega_{ms} \underline{\omega}_s\right)\right|}{\sqrt{E\left(\underline{\omega}_m^H \mathbf{T}_{mm} \underline{\omega}_m\right) E\left(\underline{\omega}_s^H \mathbf{T}_{ss} \underline{\omega}_s\right)}} \qquad (7)$$

where $E(\ldots)$ indicates the expectation operator. In order to estimate the spatial coherence, a window is required and it is assumed that the surrounding pixels in the window have similar scattering properties. Therefore, in addition to the loss of the spatial details, the optimization process will not work properly in the common case where this is not true.

The $\underline{\omega}$ vector can be constrained to be the same all along the whole stack of images. This is referred to as equal scattering mechanisms (ESM), which selects the most stable scattering mechanism over time for each pixel of an image set covering a case study [26]. Moreover, in the case of multibaseline spatial coherence optimization, the averaged spatial coherence, $\overline{\rho}$, is optimized according to the following equation:

$$|\overline{\rho}| = \frac{1}{K} \sum_{k=1}^{K} |\rho_k| \qquad (8)$$

where K is the number of interferometric pairs.

B. ESPO

Polarimetric PSI was first introduced by Navarro-Sanchez *et al.* in [23] through ESPO, which is a multibaseline ESM optimization method. This optimization approach consists of searching for the unitary vector $\underline{\omega}$ that maximizes the PS selection criteria, which can be either average spatial coherence or amplitude dispersion index. The optimum interferogram can be found with a parameterization of $\omega(\alpha, \psi)$, in the case of dual polarimetry, as

$$\underline{\omega} = [\cos\alpha, \ \sin\ \alpha e^{j\psi}]^T, \quad \begin{cases} 0 \leq \alpha \leq \pi/2 \\ -\pi \leq \psi < \pi. \end{cases} \qquad (9)$$

This parameterization of the projection vector assumes that it is unitary, $|\underline{\omega}| = 1$, and rotated such that the phase of the first element is zero. Through an exhaustive search, optimum values are found for α and ψ for each pixel. The α parameter we define here should not be confused with the α angle widely used in polarimetry after its definition in [17].

After optimization of the quality criteria, PS pixels are selected based on a threshold average spatial coherence in multilooked data, or a threshold amplitude dispersion index in single-looked data. More recently, the amplitude dispersion index was optimized through ESPO to improve the PS analysis in [27]. Moreover, an alternative way to optimize the coherence was proposed to decrease the computation time [29].

III. Temporal Coherence in StaMPS

StaMPS is a PSI technique designed to work in nonurban environments, with deformation that may be highly nonlinear in time. The PS identification step in this method is based primarily on phase characteristics and can identify low-amplitude pixels more effectively than traditional amplitude-based algorithms [9].

The main criterion of PS identification, temporal coherence, is estimated using phase analysis. After forming interferograms and removing most of topographic phase, the residual phase of the xth pixel in the kth interferogram, $\varphi_{\text{int},x,k}$, contains a contribution from several sources as

$$\varphi_{\text{int},x,k} = \varphi_{\text{def},x,k} + \varphi_{\alpha,x,k} + \varphi_{\text{orb},x,k} + \varphi_{\varepsilon,x,k} + \varphi_{n,x,k} \qquad (10)$$

where $\varphi_{\text{def},x,k}$ is the phase change due to deformation in the satellite line-of-sight (LOS) direction, $\varphi_{\alpha,x,k}$ is the phase due to difference in atmospheric delay between passes, $\varphi_{\text{orb},x,k}$ is the phase due to orbit inaccuracies, $\varphi_{\varepsilon,x,k}$ is the residual topographic phase due to error in the DEM, and $\varphi_{n,x,k}$ is the decorrelation noise term.

Quantification of the noise term is used to identify which scatterers are persistent [30]. Assuming spatial correlation of most of phase contributions over a specified distance, the spatial average of residual phase, $\bar{\varphi}_{\text{int},x,k}$, is estimated using a spatial filtering as

$$\bar{\varphi}_{\text{int},x,k} = \overline{\varphi}_{\text{def},x,k} + \overline{\varphi}_{\alpha,x,k} + \overline{\varphi}_{\text{orb},x,k} + \overline{\varphi}_{\varepsilon,x,k} \qquad (11)$$

where the bar denotes the spatially filtered phase, and $\overline{\varphi}_{\varepsilon,x,k}$ is the spatially filtered sum of $\varphi_{\varepsilon,x,k}$ and $\varphi_{n,x,k}$. Subtracting the spatially correlated phase, (11), from residual phase, (10), yields

$$\varphi_{\text{int},x,k} - \bar{\varphi}_{\text{int},x,k} = \varphi_{\varepsilon,x,k} + \varphi_{n,x,k} - \overline{\varphi}'_{\varepsilon,x,k} \qquad (12)$$

where $\overline{\varphi}'_{\varepsilon,x,k} = \overline{\varphi}_{\varepsilon,x,k} - (\varphi_{\text{def},x,k} - \overline{\varphi}_{\text{def},x,k}) - (\varphi_{\alpha,x,k} - \overline{\varphi}_{\alpha,x,k}) - (\varphi_{\text{orb},x,k} - \overline{\varphi}_{\text{orb},x,k})$, and is assumed to be insignificant. The residual topography phase is proportional to the perpendicular component of the baseline, $B_{\perp,x,k}$, so $\varphi_{\varepsilon,x,k} = B_{\perp,x,k} G_{\varepsilon,x}$ where $G_{\varepsilon,x}$ is a proportionality constant that can be estimated. Temporal coherence, which is a measure of phase noise level and indicator of whether the pixel is a PS [30], [31], is defined as follows:

$$\gamma_x = \frac{1}{K} \left| \sum_{k=1}^{K} \exp\{\sqrt{-1}(\varphi_{\text{int},x,k} - \bar{\varphi}_{\text{int},x,k} - \hat{\varphi}_{\varepsilon,x,k})\} \right| \qquad (13)$$

where K is the number of available interferograms and $\hat{\varphi}_{\varepsilon,x,k}$ is the estimate of residual topographic phase. For each PS candidate, $\bar{\varphi}_{\text{int},x,k}$, $\hat{\varphi}_{\varepsilon,x,k}$, and relevant γ_x are estimated in an iterative process until temporal coherence convergence is achieved. Finally, PS pixels are selected based on the probability that their phase time series is not just noise, by comparing

This article has been accepted for inclusion in a future issue of this journal. Content is final as presented, with the exception of pagination.

4

IEEE TRANSACTIONS ON GEOSCIENCE AND REMOTE SENSING

$$
\begin{aligned}
\varphi_{\text{opt}-int,x,k} &= \arg\left(\underline{\boldsymbol{\omega}}_m^H \Omega_{ms} \underline{\boldsymbol{\omega}}_s\right) \\
&= \arg\left(\frac{1}{2}\begin{bmatrix} \omega_m^{i*} & \omega_m^{ii*} \end{bmatrix}\begin{bmatrix} S_m^{\text{HH}+\text{VV}} \cdot S_s^{\text{HH}+\text{VV}*} & S_m^{\text{HH}+\text{VV}} \cdot S_s^{\text{HH}-\text{VV}*} \\ S_m^{\text{HH}-\text{VV}} \cdot S_s^{\text{HH}+\text{VV}*} & S_m^{\text{HH}-\text{VV}} \cdot S_s^{\text{HH}-\text{VV}*} \end{bmatrix}\begin{bmatrix} \omega_s^i \\ \omega_s^{ii} \end{bmatrix}\right) \\
&= \arg\left(f_1 \cdot \frac{1}{2}\left(S_m^{\text{HH}+\text{VV}} \cdot S_s^{\text{HH}+\text{VV}*}\right) + f_2 \cdot \frac{1}{2}\left(S_m^{\text{HH}+\text{VV}} \cdot S_s^{\text{HH}-\text{VV}*}\right) + f_3 \cdot \frac{1}{2}\left(S_m^{\text{HH}-\text{VV}} \cdot S_s^{\text{HH}+\text{VV}*}\right)\right. \\
&\quad \left. + f_4 \cdot \frac{1}{2}\left(S_m^{\text{HH}-\text{VV}} \cdot S_s^{\text{HH}-\text{VV}*}\right)\right) \\
&= \arg(f_1 \cdot \Phi_{int-1}, x, k + f_2 \cdot \Phi_{int-2}, x, k + f_3 \cdot \Phi_{int-3}, x, k + f_4 \cdot \Phi_{int-4}, x, k) \quad\quad (14)
\end{aligned}
$$

the joint probability density function of coherence and amplitude dispersion index to that for simulated pixels with random phase.

IV. TEMPORAL COHERENCE OPTIMIZATION IN POLSTAMPS

All polarimetric PSI algorithms to date have utilized spatial coherence or the amplitude dispersion index to optimize the weights for the different polarimetric channels. Amplitude-based polarimetric PSI is only useful for high amplitude PS. On the other hand, using spatial coherence to select PS pixels relies on surrounding pixels having the same mechanism, which is often not the case for PS pixels.

In our new algorithm, we extend the approach of StaMPS, which uses temporal coherence to select PS with high density in nonurban areas. The main goal of the algorithm is to find the weights for the polarimetric channels that optimize the temporal coherence for each pixel. In addition to optimizing the phase-based criterion, implementing the optimization process after forming interferograms and removing the topographic contribution is a difference of PolStaMPS compared to other polarimetric PSI algorithms.

The optimum interferogram phase, $\varphi_{\text{opt}-int,x,k}$, obtained from substituting (2) in (5), is given in (14), as shown at the top of this page, where $\Phi_{int-1,x,k}, \ldots, \Phi_{int-4,x,k}$, elements of $[\Omega_{ms}]$, are four different types of interferogram, whose linear combination forms the optimum kth interferogram for the xth pixel. $\boldsymbol{\omega}^i$ and $\boldsymbol{\omega}^{ii}$ are the first and second elements of $\underline{\boldsymbol{\omega}}$. $f_1, \ldots, f_4$ are the coefficients for the four types of interferogram as

$$
\begin{aligned}
f_1 &= \omega_m^{i*} \cdot \omega_s^i \\
f_2 &= \omega_m^{ii*} \cdot \omega_s^i \\
f_3 &= \omega_m^{i*} \cdot \omega_s^{ii} \\
f_4 &= \omega_m^{ii*} \cdot \omega_s^{ii}.
\end{aligned} \quad\quad (15)
$$

The polarimetric expression of temporal coherence is introduced in (16). Similar to standard StaMPS, there is an iterative process to estimate $\bar{\varphi}_{\text{opt}-int,x,k}$, which is substituted by the spatially correlated phase of $\Phi_{int-1,x,k}$ in the first iteration. In every iteration, after applying a spatial filtering to calculate $\bar{\varphi}_{\text{opt}-int,x,k}$, the optimum values for $f_1, \ldots, f_4$ and $\hat{\varphi}_{\varepsilon,x,k}$ are found in the defined search spaces to optimize $\gamma_{\text{pol},x}$ and then the final value of the $\hat{\varphi}_{\varepsilon,x,k}$ is estimated through the obtained optimum phase. In the final iteration, polarimetric temporal coherence converges, and the coefficients and the optimum

interferograms, according to (14), are obtained

$$
\gamma_{\text{pol},x} = \frac{1}{K}\left|\sum_{k=1}^{K}\exp\{\sqrt{-1}(\varphi_{\text{opt-int},x,k} - \bar{\varphi}_{\text{opt-int},x,k} - \hat{\varphi}_{\varepsilon,x,k})\}\right|. \quad\quad (16)
$$

In order to optimize $\gamma_{\text{pol},x}$, the coefficients are parametrised based on the definition of $\underline{\boldsymbol{\omega}}$ in ESPO as

$$
\begin{aligned}
f_1 &= \cos\alpha \cdot \cos\alpha = \cos\alpha^2 \\
f_2 &= \sin\alpha\, e^{-j\psi} \cdot \cos\alpha = \sin\alpha \cdot \cos\alpha \cdot e^{-j\psi} \\
f_3 &= \cos\alpha \cdot \sin\alpha\, e^{j\psi}\cos\alpha \cdot \sin\alpha\, e^{j\psi} \\
f_4 &= \sin\alpha\, e^{-j\psi} \cdot \sin\alpha\, e^{j\psi} = \sin\alpha^2.
\end{aligned} \quad\quad (17)
$$

Therefore, only a 2-D search space is defined by α and ψ in each iteration, and the best values are extracted for each one. In order to define the coefficients and then optimize the temporal coherence, we specified a grid for the search space of α and ψ values, with $10°$ steps. Steps larger than $10°$ would yield a shorter computing time, but due to the relatively complex pattern of the temporal coherence function, may cause convergence on a local maximum rather than the absolute one.

V. CASE STUDY AND DATA SET

Since the main priority of this research is increasing PS density in nonurban areas, we selected Tehran basin, which contains areas primarily covered by vegetation, as a test case. The Tehran basin suffers from a high rate of land subsidence and is located in the north of Iran, between the Alborz Mountains to the north and the Arad and Fashapouye mountains to the south. This subsidence was first revealed by geodetic observations from precise leveling surveys carried out across the area between 1995 and 2002 [32]. Due to poor coherence, conventional interferometry has generally not been successful in measuring deformation. Therefore, a number of enhanced algorithms based on PSI have been applied to this region [33], [34], [35]. We applied our new PolStaMPS method to a 2.6×1.2 km portion of the Tehran basin containing pixels with the highest rate of deformation and covered mostly by agricultural fields (Fig. 1).

In order to optimize the temporal coherence using polarimetric data, we tasked TerraSAR-X to acquire dual-polarization (HH/VV) images. A set of 22 dual-polarization strip-map images from July 21, 2013 to April 22, 2014 were obtained. Azimuth and slant-range resolutions are 6.6 and 1.17 m, respectively, whereas the pixel dimensions are 2.4 and

This article has been accepted for inclusion in a future issue of this journal. Content is final as presented, with the exception of pagination.

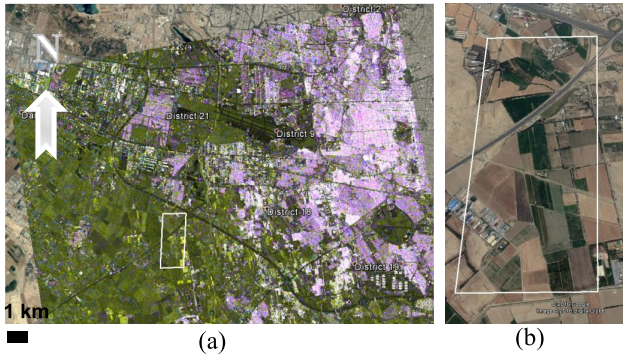SADEGHI *et al.*: NEW POLARIMETRIC PS INTERFEROMETRY METHOD

5

Fig. 1. (a) Spatial location of the case study (outlined polygon) over the composite RGB of master image (20131211), Channels: R = HH, G = VV, B: Absolute value of the difference between channels. (b) Case study (outlined rectangle) with detailed features.
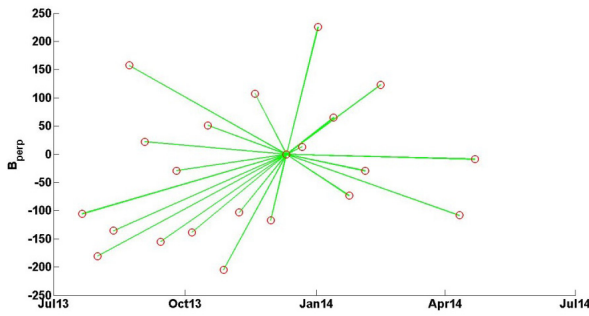

Fig. 2. Spatial baselines versus temporal baselines of slave images with respect to the master (20131211).

0.91 m, respectively. Fig. 2 illustrates the spatial and temporal baselines of all slave images with respect to the master one.

VI. POLSTAMPS RESULTS AND DISCUSSION

In addition to the linear channels (HH and VV), we also ran StaMPS on the HH+VV channel, which forms the initial copolar interferogram in PolStaMPS, $\Phi_{\text{int}-1,x,k}$, as its phase values are expected to be more stable over surface scattering areas, e.g., rural ones, than the linear channels.

Fig. 3 displays the polarimetric temporal coherence values as a function of (α, ψ) for four representative pixels with different values of optimum temporal coherence. The shape of the temporal coherence function is smooth enough to allow numerical methods to approximate the maximum value. For this reason, a point close to the absolute maximum of the temporal coherence is first found using a grid search, and then a gradient-based method is used to find the maximum, hence reducing the computational cost.

Histograms of the estimated $\gamma_{\text{pol},x}$ in PolStaMPS and the estimated γ_x in standard StaMPS for initial selected pixels are compared in Fig. 4. This comparison shows a significant increase in the number of pixels with high temporal coherence for the optimum channel, compared to the HH, VV, and HH+VV channels. The increase in coherence will be, in part, due to an increase in the bias. For instance, coherence estimated on the sea is not zero (as it should be theoretically) due to the estimation bias in any single channel and, moreover, increases in the optimum polarimetric combination. To test
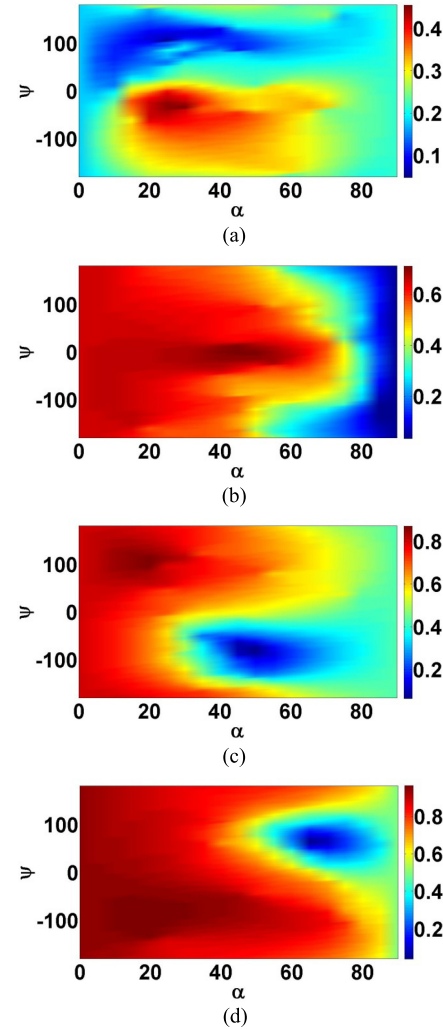

Fig. 3. Temporal coherence values as a function of (α, ψ) for four representative pixels with different values of $\gamma_{\text{pol},x}$. (a) $\gamma_{\text{pol},x} = 0.456$. (b) $\gamma_{\text{pol},x} = 0.711$. (c) $\gamma_{\text{pol},x} = 0.871$. (d) $\gamma_{\text{pol},x} = 0.962$.
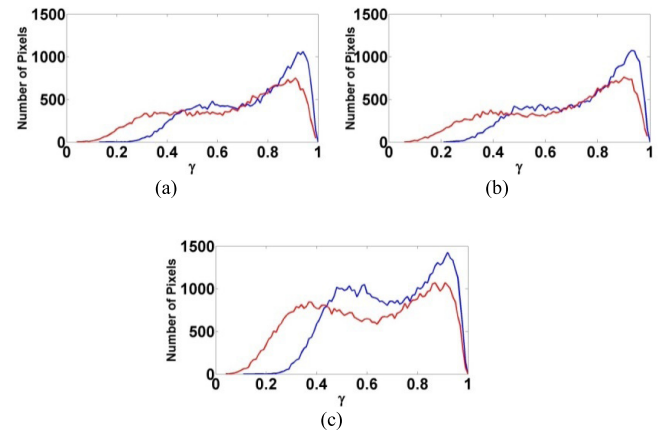

Fig. 4. Histogram of the γ_x and the $\gamma_{\text{pol},x}$ for initial selected pixels related to (a) HH and Optimum channel, (b) VV and Optimum channel, and (c) HH+VV and optimum channel. Blue line: optimum channel behavior. Red line: single-pol channel behavior.

whether the entire coherence increase can be explained by an increase in the bias, we check (below) the spatial distribution
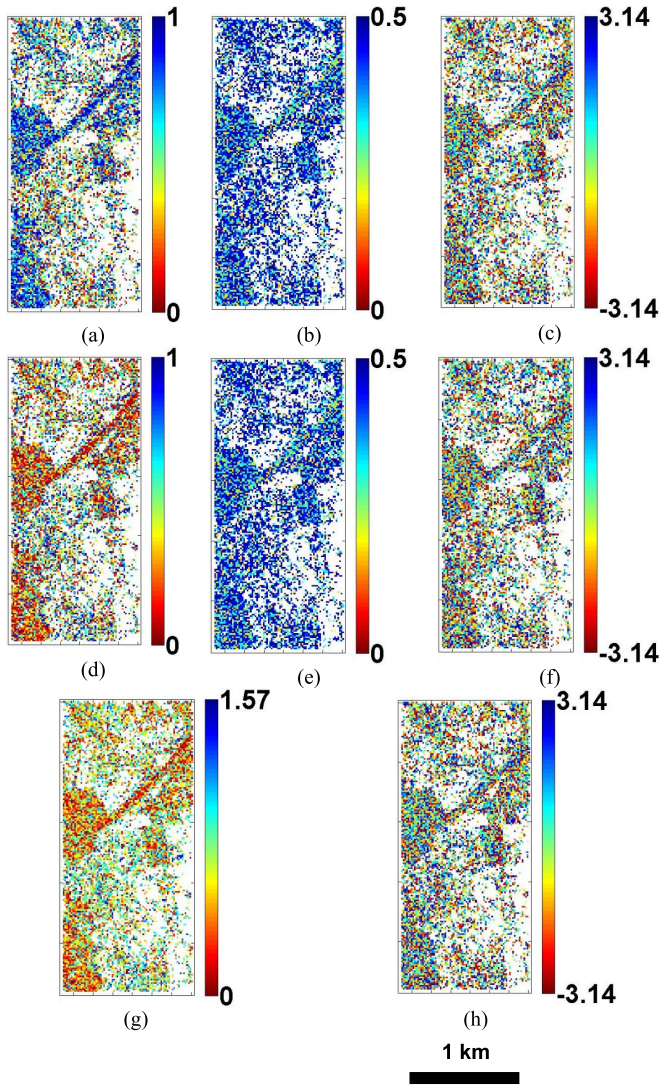
This article has been accepted for inclusion in a future issue of this journal. Content is final as presented, with the exception of pagination.

6   IEEE TRANSACTIONS ON GEOSCIENCE AND REMOTE SENSING

Fig. 5. Maps of optimum coefficients and parameters for an interferogram. (a) f_1. (b) Amplitude of f_2. (c) Phase of f_2. (d) f_4. (e) Amplitude of f_3. (f) Phase of f_3. (g) α. (h) ψ.

TABLE I
NUMBER OF IDENTIFIED PS PIXELS

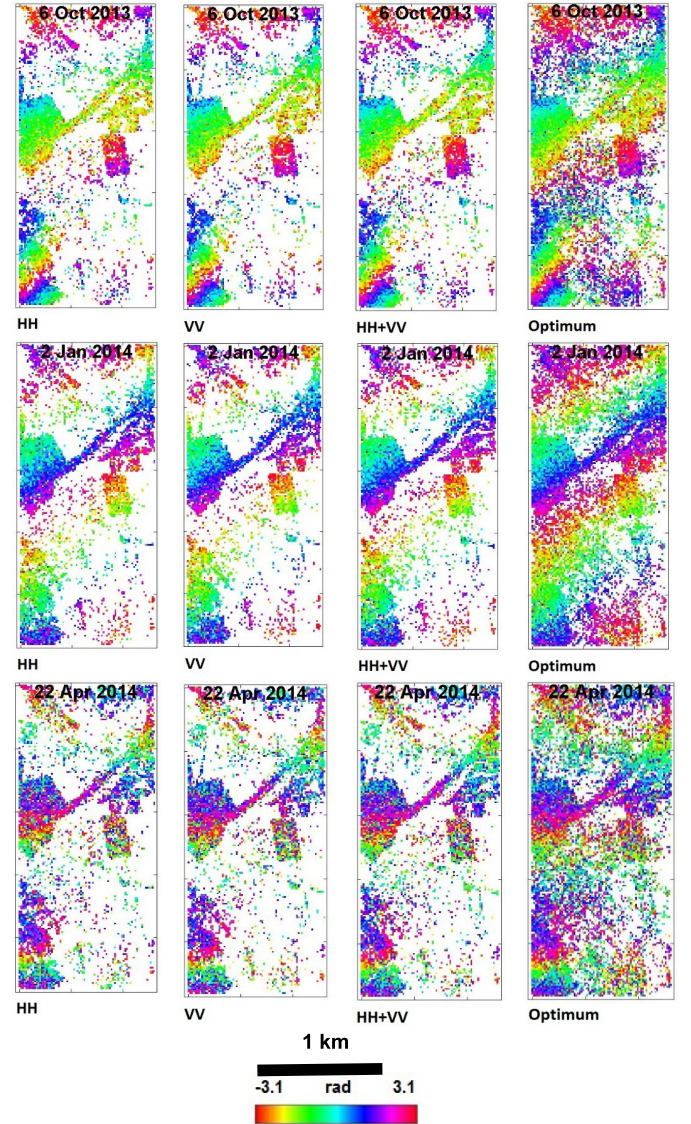| HH	VV	HH+VV	Optimum
26322	26694	32374	47997

Fig. 6. Selection of wrapped interferograms formed from available data set acquired using HH, VV, HH+VV, and Optimum channel over the case study. The master acquisitions date is Dec 11, 2013. Each color fringe represents 1.55 cm of displacement in the LOS.

of the optimum coefficients, and compare the noise levels of selected points in the original channels to those in the optimum channel. We note, however, that in any case, the increase in bias should not lead to more pixels being selected, due to the StaMPS mechanism for pixel selection, which depends on a comparison of the coherence distribution to that for simulated pixels, rather than simple thresholding.

In homogeneous areas, the scattering properties of neighboring pixels are expected to be spatially similar. Therefore, if the projection vectors and the optimum coefficients reflect the actual scattering properties, rather than taking values that just increase the coherence bias of each pixel, they will generally be spatially smooth.

As can be seen in Fig. 5, the estimated coefficients are not randomly distributed, and there is spatial consistency for the distribution of all coefficients, especially f_1 and f_4, which are real numbers and correspond to the two copolar interferograms. The coefficient of the first copolar interferogram, f_1, which enhances the surface scattering behavior, has large values in most of the areas. Moreover, a clear complementarity between f_1 and f_4 is observed, where f_1 is

small, f_4 is large. f_2 and f_3 are complex coefficients for the two cross-polar interferograms, and their maps are similar for amplitude and phase.

The number of final selected PS pixels over the case study using standard StaMPS for different channels (HH, VV, and HH+VV) and PolStaMPS is presented in Table I. It is clear that the increase in the number of PS pixels using the HH+VV channel in standard StaMPS compared to the linear channels is trivial. However, using PolStaMPS, the number increases by 48%, 80%, and 82% with respect to HH+VV, VV, and HH channels, respectively. There are some PS pixels which are

This article has been accepted for inclusion in a future issue of this journal. Content is final as presented, with the exception of pagination.

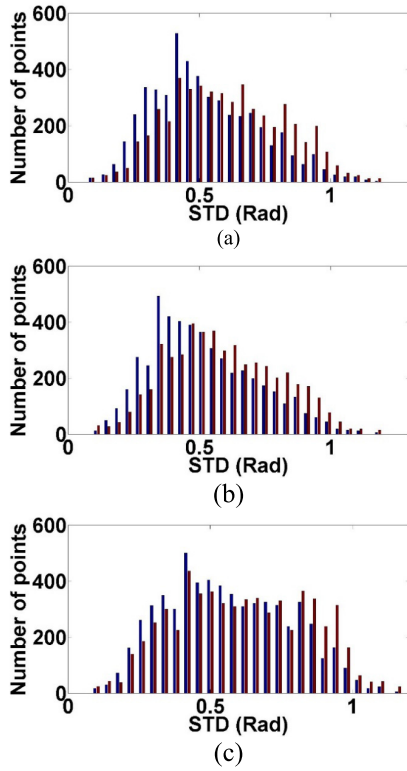SADEGHI *et al.*: NEW POLARIMETRIC PS INTERFEROMETRY METHOD
7

Fig. 7. Histogram of phase noise standard deviation for commonly identified PS pixels between the optimum channel and (a) HH channel, (b) VV channel, and (c) HH+VV channel. Blue Bar: optimum channel behavior. Red bar: single-polar channel behavior.
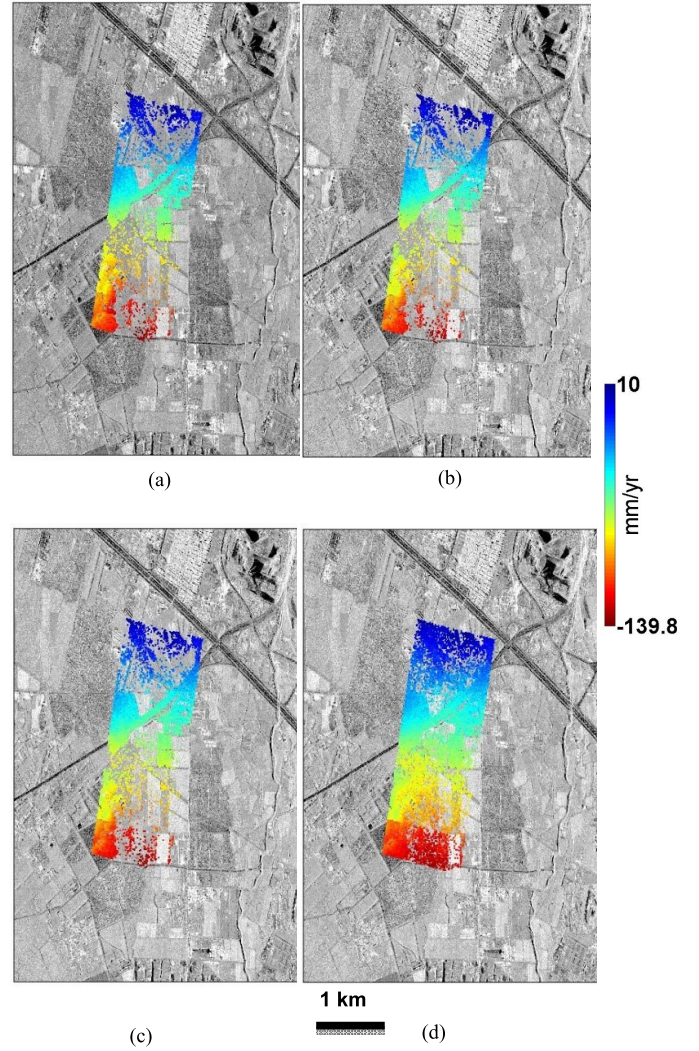

Fig. 8. Mean LOS velocities on the case study between July 21, 2013 and April 22, 2014 plotted on interferogram amplitude. (a) HH channel. (b) VV channel. (c) HH+VV channel. d) Optimum channel.

not identified by StaMPS with linear channels, but they are selected by both PolStaMPS and StaMPS with HH+VV. In fact, approximately 40% of the additional PS pixels that are selected by PolStaMPS with respect to StaMPS with linear channels are also selected by StaMPS with HH+VV channel.

Fig. 6 shows the wrapped phase of selected pixels for optimum, HH, VV, and HH+VV interferograms. As can be seen, the additional PS pixels in the optimum channel look clearly coherent. Furthermore, there are some common PS pixels whose phases are less noisy in the optimum interferogram. In order to assess the phase quality for the interferograms obtained by PolStaMPS in comparison to the original StaMPS, phase noise is estimated according to [9]. First, the PS pixels are connected to form a network using Delaunay triangulation. Then, for each arc connecting two PS pixels, a weighted-average phase is calculated from the entire time series, and removed from the original phase of the arc, which is then low-pass filtered in time. The resulting phase, with the weighted-average phase added back in, provides an estimate for the smooth underlying signal. Phase noise is estimated by subtracting the smooth phase from the original phase of the arc. Finally, the phase noise of each PS pixel is obtained from the phase noise of its corresponding arcs. Fig. 7 shows a comparison of histograms of phase noise standard deviation for commonly identified PS pixels in single-polar and optimum channels. The optimum channel shows a 7%, 16%, and 17% reduction in the number of PS pixels with standard deviation above 0.5 radians with respect to HH+VV, VV, and HH channels. This confirms that in addition to increasing PS

density, the proposed algorithm is also successful in reducing the noise level of those PS pixels selected by standard StaMPS, although the reduction in the noise level is less pronounced than the increase in the number of selected PS pixels.

The resulting velocity maps of PolStaMPS and standard StaMPS are plotted in Fig. 8. The pattern of deformation rate is very similar, as expected, but the density of measurements is greater in the PolStaMPS case. The maximum velocity for this case study is -139.7 mm/year for the optimum channel.

The polarimetric PSI method leads to an increase in the number of selected PS pixels when compared to standard PSI, although this comes with a computational cost. PolStaMPS is inspired by ESPO and consequently finds the coefficients in the defined search spaces to optimize the temporal coherence. This leads to an increase in the computation time of $\sim$80 times with respect to standard StaMPS. The computation time depends on the defined step in the search spaces; larger steps decrease the computation time, although they could lead to convergence on local optima instead of global ones. Optimizing the temporal coherence using other existing

optimization methods, e.g., Union, in which the optimum channel is selected from a polarimetric channel with limited availability [21], may work with a lower computational cost, but the solutions are suboptimal. It should be mentioned that PolStaMPS can be applied over areas larger than the case study in this research, and the computation cost increases approximately linearly with the number of pixels of the scene.

VII. Conclusion

In this paper, we present a new polarimetric PSI approach that 1) is applicable in areas lacking man-made structures and 2) retains the full spatial resolution of the input images. Using this technique, we are able to identify the natural targets that the standard PSI approach fails to select: the number of PS is improved by 48%, 80%, and 82% with respect to the HH+VV, VV, and HH channels, respectively. Moreover, the phase quality of the selected PS pixels is also improved. We have successfully applied this new algorithm to a rural part of the Tehran basin to monitor high-rate land subsidence and envisage that it can be used to estimate crustal deformation in most terrains. Future work should include a comparison of the results and performance of PolStaMPS with respect to other polarimetric PSI methods.

References

[1] A. Ferretti, C. Prati, and F. Rocca, "Permanent scatterers in differential SAR interferometry," *IEEE Trans. Geosci. Remote Sens.*, vol. 38, no. 5, pp. 2202–2212, Sep. 2000.

[2] A. Ferretti, C. Prati, and F. Rocca, "Permanent scatterers in SAR interferometry," *IEEE Trans. Geosci. Remote Sens.*, vol. 39, no. 1, pp. 8–20, Jan. 2001.

[3] C. Colesanti, A. Ferretti, F. Novali, C. Prati, and F. Rocca, "SAR monitoring of progressive and seasonal ground deformation using the permanent scatterers technique," *IEEE Trans. Geosci. Remote Sens.*, vol. 41, no. 7, pp. 1685–1701, Jul. 2003.

[4] S. Lyons and D. Sandwell, "Fault creep along the southern San Andreas from interferometric synthetic aperture radar," *J. Geophys. Res.*, vol. 108, no. B1, p. 2047, 2003.

[5] C. Werner, U. Wegmuller, T. Strozzi, and A. Wiesmann, "Interferometric point target analysis for deformation mapping," in *Proc. IGARSS*, Jul. 2003, pp. 4362–4364.

[6] B. Kampes, "Displacement parameter estimation using permanent scatterer interferometry," Ph.D. dissertation, Faculty Civil Eng. Geosci., Delft Univ. Technol., Delft, The Netherlands, 2005.

[7] P. Berardino, G. Fornaro, R. Lanari, and E. Sansosti, "A new algorithm for surface deformation monitoring based on small baseline differential SAR interferograms," *IEEE Trans. Geosci. Remote Sens.*, vol. 40, no. 11, pp. 2375–2383, Nov. 2002.

[8] R. Lanari, O. Mora, M. Manunta, J. J. Mallorquí, P. Berardino, and E. Sansosti, "A small-baseline approach for investigating deformations on full-resolution differential SAR interferograms," *IEEE Trans. Geosci. Remote Sens.*, vol. 42, no. 7, pp. 1377–1386, Jul. 2004.

[9] A. Hooper, H. Zebker, P. Segall, and B. Kampes, "A new method for measuring deformation on volcanoes and other natural terrains using InSAR persistent scatterers," *Geophys. Res. Lett.*, vol. 31, p. L23611, 2004.

[10] R. Bamler and D. Just, "Phase statistics and decorrelation in SAR interferograms," in *Proc. Better Understand. Earth Environ., Int. Geosci. Remote Sens. Symp. (IGARSS)*, Tokyo, Japan, Aug. 1993, pp. 980–984.

[11] J.-S. Lee and E. Pottier, *Polarimetric Radar Imaging: From Basics to Applications*. Boca Raton, FL, USA: CRC Press, 2009.

[12] S. Cloude, *Polarisation: Applications in Remote Sensing*, London, U.K.: Oxford Univ. Press, 2009.

[13] J.-S. Lee, K. W. Hoppel, S. A. Mango, and A. R. Miller, "Intensity and phase statistics of multilook polarimetric and interferometric SAR imagery," *IEEE Trans. Geosci. Remote Sens.*, vol. 32, no. 5, pp. 1017–1028, Sep. 1994.

[14] J. J. Van Zyl and C. F. Burnette, "Bayesian classification of polarimetric SAR images using adaptive *a priori* probabilities," *Int. J. Remote Sens.*, vol. 13, no. 5, pp. 835–840, 1992.

[15] A. Freeman and S. L. Durden, "A three-component scattering model for polarimetric SAR data," *IEEE Trans. Geosci. Remote Sens.*, vol. 36, no. 3, pp. 963–973, May 1998.

[16] J. J. Van Zyl, "Unsupervised classification of scattering behavior using radar polarimetry data," *IEEE Trans. Geosci. Remote Sens.*, vol. 27, no. 1, pp. 36–45, Jan. 1989.

[17] S. R. Cloude and E. Pottier, "A review of target decomposition theorems in radar polarimetry," *IEEE Trans. Geosci. Remote Sens.*, vol. 34, no. 2, pp. 498–518, Mar. 1996.

[18] S. R. Cloude and K. P. Papathanassiou, "Polarimetric SAR interferometry," *IEEE Trans. Geosci. Remote Sens.*, vol. 36, no. 5, pp. 1551–1565, Sep. 1998.

[19] M. Neumann, L. Ferro-Famil, and A. Reigber, "Multibaseline polarimetric SAR interferometry coherence optimization," *IEEE Geosci. Remote Sens. Lett.*, vol. 5, no. 1, pp. 93–97, Jan. 2008.

[20] E. Colin, C. Titin-Schnaider, and W. Tabbara, "An interferometric coherence optimization method in radar polarimetry for high-resolution imagery," *IEEE Trans. Geosci. Remote Sens.*, vol. 44, no. 1, pp. 167–175, Jan. 2006.

[21] L. Pipia *et al.*, "Polarimetric differential SAR interferometry: First results with ground-based measurements," *IEEE Geosci. Remote Sens. Lett.*, vol. 6, no. 1, pp. 167–171, Jan. 2009.

[22] L. Pipia, X. Fabregas, A. Aguasca, C. Lopez-Martinez, and J. J. Mallorquí, "Polarimetric coherence optimization for interferometric differential applications," in *Proc. IGARSS*, Jul. 2009, pp. V-146–V-149.

[23] V. D. Navarro-Sanchez, J. M. Lopez-Sanchez, and F. Vicente-Guijalba, "A contribution of polarimetry to satellite differential SAR interferometry: Increasing the number of pixel candidates," *IEEE Geosci. Remote Sens. Lett.*, vol. 7, no. 2, pp. 276–280, Apr. 2010.

[24] R. Iglesias, D. Monells, X. Fabregas, J. J. Mallorqui, A. Aguasca, and C. López-Martinez, "Phase quality optimization in polarimetric differential SAR interferometry," *IEEE Trans. Geosci. Remote Sens.*, vol. 52, no. 5, pp. 2875–2888, May 2014.

[25] Z. Sadeghi, M. J. V. Zoej, and J. P. Müller, "Monitoring land subsidence in a rural area using a combination of ADInSAR and polarimetric coherence optimization," *IEEE J. Sel. Topics Appl. Earth Observ. Remote Sens.*, vol. 10, no. 8, pp. 3582–3590, Aug. 2017.

[26] V. D. Navarro-Sanchez, J. M. Lopez-Sanchez, and L. Ferro-Famil, "Polarimetric approaches for persistent scatterers interferometry," *IEEE Trans. Geosci. Remote Sens.*, vol. 52, no. 3, pp. 1667–1676, Mar. 2014.

[27] M. Esmaeili and M. Motagh, "Improved persistent scatterer analysis using amplitude dispersion index optimization of dual polarimetry data," *ISPRS J. Photogram. Remote Sens.*, vol. 117, pp. 108–114, Jul. 2016.

[28] J. J. Van Zyl, H. A. Zebker, and C. Elachi, "Imaging radar polarization signatures: Theory and observation," *Radio Sci*, vol. 22, no. 4, pp. 529–543, 1987.

[29] B. Wu, T. Ling, Y. Chen, and H. Lei, "New methods in multibaseline polarimetric SAR interferometry coherence optimization," *IEEE Geosci. Remote Sens. Lett.*, vol. 12, no. 10, pp. 2016–2020, Oct. 2015.

[30] A. Hooper, P. Segall, and H. Zebker, "Persistent scatterer interferometric synthetic aperture radar for crustal deformation analysis with application to Volcan Alcedo, Galapagos," *J. Geophys. Res.*, vol. 112, p. B07407, 2007.

[31] A. Hooper, "Persistent scatterer RADAR interferometry for crustal deformation studies and modeling of volcanic deformation," Ph.D. dissertation, Dept. Geophys., Stanford Univ., Stanford, CA, USA, 2006.

[32] M. Amighpey, S. Arabi, A. Talebi, and D. Jamour, "Elevation changes of the precise leveling tracks in the Iran leveling network," Nat. Cartographic Center (NCC) Iran, Tehran, Iran, Tech. Rep., 2006.

[33] Z. Sadeghi, M. J. Valadan Zoej, M. Dehghani, and N.-B. Chang, "Enhanced algorithm based on persistent scatterer interferometry for the estimation of high-rate land subsidence," *J. Appl. Remote Sens.*, vol. 6, p. 063573, Sep. 2012.

[34] Z. Sadeghi, M. J. Valadan Zoej, and M. Dehghani, "An improved persistent scatterer interferometry for subsidence monitoring in the tehran basin," *IEEE J. Sel. Topics Appl. Earth Observat. Remote Sens.*, vol. 6, no. 3, pp. 1571–1577, Jun. 2013.

[35] M. Dehghani, M. J. V. Zoej, A. Hooper, R. F. Hanssen, I. Entezam, and S. Saatchi, "Hybrid conventional and persistent scatterer SAR interferometry for land subsidence monitoring in the Tehran Basin, Iran," *ISPRS J. Photogram. Remote Sens.*, vol. 79, pp. 157–170, May 2013.

Zahra Sadeghi received the M.S. and Ph.D. degrees in remote sensing from the K. N. Toosi University of Technology, Tehran, Iran, in 2011 and 2017, respectively, with a focus on developing performance of persistent scatterer InSAR (PSI) techniques for crustal deformation mapping.

From 2011 to 2014, she was with the Remote Sensing Research Center, K. N. Toosi University of Technology, where she was involved in the preparation of instructions for feature extraction from satellite images. From 2015 to 2017, she was a Visiting Ph.D. Student with the University College London, London, U.K., where she was involved in the combination of PSI and polarimetric coherence optimization methods.

Her research interests include advanced InSAR processing to monitor geohazards and polarimetric InSAR methods to improve performance of interferometric processing.

Mohammad Javad Valadan Zoej received the Ph.D. degree in remote sensing and photogrammetry from the University of Glasgow, Glasgow, U.K., in 1997.

He is currently a Professor with the Faculty of Geodesy and Geomatics, K. N. Toosi University of Technology, Tehran, Iran. His research interests include 3-D spatial information extraction from space images, hyperspectral and multispectral image processing, automatic feature extraction, radargrammetry, and interferometry.

Andrew Hooper (M'09–SM'12) received the M.S. and Ph.D. degrees in geophysics from Stanford University, Stanford, CA, in 2002 and 2006, respectively, for his development of SAR persistent scatterer interferometry algorithms for geophysical applications.

Between 2002 and 2003, he worked at the German Space Center (DLR) on algorithms for the TerraSAR-X satellite. From 2006, he was at the University of Iceland, before moving to Delft University of Technology in 2008. Since 2013 he is Professor of Geophysics and Geodesy at the University of Leeds. His current research interests include imaging and modeling magma movement at volcanoes, slip on faults, and the solid Earth response to retreating glaciers.

Juan M. Lopez-Sanchez (S'94–M'00–SM'05) was born in Alicante, Spain, in 1972. He received the M.S. and Ph.D. degrees in telecommunication engineering from the Technical University of Valencia, Valencia, Spain, in 1996 and 2000, respectively.

From 1998 to 1999, he was a Pre-Doctoral Grant Holder with the Space Applications Institute, Joint Research Centre of the European Commission, Ispra, Italy. Since 2000, he has been the Leader of the Signals, Systems, and Telecommunication Group, University of Alicante, Alicante, Spain, where he has also been a Full Professor since 2011. He has co-authored more than 60 papers in refereed journals and more than 110 papers and presentations in international conferences and symposia.

His research interests include microwave remote sensing for inversion of biophysical parameters, polarimetric and interferometric techniques, synthetic aperture radar imaging algorithms, and applications of radar remote sensing in agriculture and geophysics.

Dr. Lopez-Sanchez was the Chair of the Spanish Chapter of the IEEE Geoscience and Remote Sensing Society from 2006 to 2012. He was a recipient of the Indra Award for the best Ph.D. thesis about radar in Spain in 2001.